RELATIVISTIC FLOWS USING SPATIAL AND TEMPORAL ADAPTIVE STRUCTURED MESH REFINEMENT. I. HYDRODYNAMICS

Peng Wang, Tom Abel and Weiqun Zhang
Kavli Institute for Particle Astrophysics and Cosmology
Stanford Linear Accelerator Center and Stanford Physics Department, Menlo Park, CA 94025
Draft version March 30, 2007

ABSTRACT

Astrophysical relativistic flow problems require high resolution three-dimensional numerical simulations. In this paper, we describe a new parallel three-dimensional code for simulations of special relativistic hydrodynamics (SRHD) using both spatially and temporally structured adaptive mesh refinement (AMR). We used method of lines to discrete SRHD equations spatially and used a total variation diminishing (TVD) Runge-Kutta scheme for time integration. For spatial reconstruction, we have implemented piecewise linear method (PLM), piecewise parabolic method (PPM), third order convex essentially non-oscillatory (CENO) and third and fifth order weighted essentially non-oscillatory (WENO) schemes. Flux is computed using either direct flux reconstruction or approximate Riemann solvers including HLL, modified Marquina flux, local Lax-Friedrichs flux formulas and HLLC. The AMR part of the code is built on top of the cosmological Eulerian AMR code *enzo*, which uses the Berger-Colella AMR algorithm and is parallel with dynamical load balancing using the widely available Message Passing Interface library. We discuss the coupling of the AMR framework with the relativistic solvers and show its performance on eleven test problems.

Subject headings: hydrodynamics–methods:numerical–relativity

1. INTRODUCTION

Relativistic flow problems are important in many astrophysical phenomena including gamma-ray burst (GRB), active galactic nuclei (AGN), as well as microquasar and pulsar wind nebulae, among others. Apparent superluminal motion is observed in many jets of extragalactic radio sources associated with AGN. According to the currently accepted standard model, this implies the jet flow velocities as large as 99% of the speed of light (Blandford et al. 1977; Begelman et al. 1984). Similar phenomena are also seen in microquasars such as GRS 1915+105 (Mirabel & Rodriguez 1994) and GRO J1655-40 (Tingay et al. 1995) thus by similar arguments relativistic flows are thought to play a role. In the case of GRB, the observed non-thermal spectrum implies that the source must be optically thin, which can be used to put a limit on the minimum Lorentz factor within those bursts (Lithwick & Sari 2001). This argument shows that the source of GRB must be in highly relativistic motion. This conclusion is further confirmed by the rapidly increasing number of GRB afterglow observations by the Swift satellite (Gehrels et al. 2004). To understand physical processes in those phenomena quantitatively, high resolution multi-dimensional simulations are crucial.

Jim Wilson and collaborators pioneered the numerical solution of relativistic hydrodynamics equations (Wilson 1972; Centrella & Wilson 1984; Hawley et al. 1984a,b). Starting with these earliest papers this has typically been done in the context of general relativistic problems such as accretion onto black holes and supernovae explosions. The problem was recognized to be difficult to solve when the Lorentz factor becomes large (Norman & Winkler 1986) and a solution with an implicit adaptive scheme

was demonstrated in one dimension. This approach is not generalizable to multi-dimension. However, in the past two decades accurate solvers based on Godunov's scheme have been designed that have adopted shock-capturing schemes for Newtonian fluid to the relativistic fluid equations in conservation form (for a review see Martí & Müller 2003). Such schemes, called high-resolution shock-capturing (HRSC) methods, have been proven to be very useful in capturing strong discontinuities with a few numerical zones without serious numerical oscillations. We will discuss a number of them in section 3.

Studies involving astrophysical fluid dynamics in general are benefiting tremendously from using spatial and temporal adaptive techniques. Smoothed particle hydrodynamics (Gingold & Monaghan 1977; Lucy 1977) is a classic example by being a Lagrangian method. Increasingly also variants of Berger & Colella (1989) are being implemented. This is also true in relativistic hydrodynamics (Hughes et al. 2002; Anninos et al. 2005; Zhang & MacFadyen 2006; Morsony et al. 2006; Meliani et al. 2007) where certainly the work of Hughes et al. (2002) showed that a serial AMR code could solve problems even highly efficient parallel fixed grid codes would have difficulty with. In this first paper of a series we discuss our implementation of different hydrodynamics solvers with various reconstruction schemes as well as different time integrators on top of the *enzo* framework previously developed for cosmology (Bryan & Norman 1997a,b; Bryan et al. 2001; O'Shea et al. 2004). This new code we call *renzo* is adaptive in time and space and is a dynamically load balanced parallel using the standard message passing interface. The next papers will discuss the extensions to relativistic ideal magnetohydrodynamics and more physics modules. In the following we briefly summarize the equations be-

Electronic address: pengwang, tabel@stanford.edu, wqzhang@slac.stanford.edu

ing solved before we give details on the different solvers we have implemented. Section 4 discusses the adaptive mesh refinement strategy and implementation. We then move on to describe various test problems for relevant combinations of solvers, reconstruction schemes in one, two and three dimensions, with and without AMR. Section 6 presents an application of our code to three-dimensional relativistic and supersonic jet propagation problem before we summarize in section 7.

2. EQUATIONS OF SPECIAL RELATIVISTIC HYDRODYNAMICS

The basic equations of special relativistic hydrodynamics (SRHD) are conservation of rest mass and energy-momentum:

$$(\rho u^\mu)_{;\mu} = 0, \tag{1}$$

and

$$T^{\mu\nu}_{\;\;;\nu} = 0, \tag{2}$$

where ρ is the rest mass density measured in the fluid frame, $u^\mu = W(1, v^i)$ is the fluid four-velocity (assuming the speed of light $c = 1$), W is the Lorentz factor, v^i is the coordinate three-velocity, $T^{\mu\nu}$ is the energy-momentum tensor of the fluid and semicolon denotes covariant derivative.

For a perfect fluid the energy-momentum tensor is

$$T^{\mu\nu} = \rho h u^\mu u^\nu + p g^{\mu\nu}, \tag{3}$$

where $h = 1 + \epsilon + p/\rho$ is the relativistic specific enthalpy, ϵ is the specific internal energy, p is the pressure and $g^{\mu\nu}$ is the spacetime metric.

SRHD equations can be written in the form of conservation laws

$$\frac{\partial U}{\partial t} + \sum_{j=1}^{3} \frac{\partial F^j}{\partial x^j} = 0, \tag{4}$$

where the conserved variable U is given by

$$U = (D, S^1, S^2, S^3, \tau)^T, \tag{5}$$

and the fluxes are given by

$$F^j = (Dv^j, S^1 v^j + p\delta^j_{\;1}, S^2 v^j + p\delta^j_{\;2}, S^3 v^j + p\delta^j_{\;3}, S^j - Dv^j)^T. \tag{6}$$

Anile (1989) has shown that system (4) is hyperbolic for causal EOS, i.e., those satisfying $c_s < 1$ where the local sound speed c_s is defined as

$$c_s^2 = \frac{1}{h}\left[\frac{\partial p}{\partial \rho} + \left(\frac{p}{\rho^2}\right)\frac{\partial p}{\partial \epsilon}\right]. \tag{7}$$

The eigenvalues and left and right eigenvectors of the characteristic matrix $\partial F / \partial U$, which are used in some of our numerical schemes, are given by Donat et al. (1998).

The conserved variables U are related to the primitive variables by

$$D = \rho W, \tag{8}$$
$$S^j = \rho h W^2 v^j, \tag{9}$$
$$\tau = \rho h W^2 - p - \rho W, \tag{10}$$

where $j = 1, 2, 3$. The system (4) are closed by an equation of state (EOS) given by $p = p(\rho, \epsilon)$. For an ideal gas, the EOS is,

$$p = (\Gamma - 1)\rho\epsilon, \tag{11}$$

where Γ is the adiabatic index.

3. NUMERICAL SCHEMES FOR SRHD

3.1. *Time Integration*

We use method of lines to discretize the system (4) spatially,

$$\frac{dU_{i,j,k}}{dt} = -\frac{F^x_{i+1/2,j,k} - F^x_{i-1/2,j,k}}{\Delta x} \tag{12}$$

$$-\frac{F^y_{i,j+1/2,k} - F^y_{i,j-1/2,k}}{\Delta y}$$

$$-\frac{F^z_{i,j,k+1/2} - F^z_{i,j,k-1/2}}{\Delta z} \equiv L(U), \tag{13}$$

where i, j, k refers to the discrete cell index in x, y, z directions, respectively. $F^x_{i\pm1/2,j,k}$, $F^y_{i,j\pm1/2,k}$ and $F^z_{i,j,k\pm1/2}$ are the fluxes at the cell interface.

As discussed by Shu & Osher (1988), if using a high order scheme to reconstruct flux spatially, one must also use the appropriate multi-level total variation diminishing (TVD) Runge-Kutta schemes to integrate the ODE system (13). Thus we implemented the second and third order TVD Runge-Kutta schemes coupled with AMR.

The second order TVD Runge-Kutta scheme reads,

$$U^{(1)} = U^n + \Delta t L(U^n), \tag{14}$$

$$U^{n+1} = \frac{1}{2}U^n + \frac{1}{2}U^{(1)} + \frac{1}{2}\Delta t L(U^{(1)}), \tag{15}$$

and the third order TVD Runge-Kutta scheme reads,

$$U^{(1)} = U^n + \Delta t L(U^n) \tag{16}$$

$$U^{(2)} = \frac{3}{4}U^n + \frac{1}{4}U^{(1)} + \frac{1}{4}\Delta t L(U^{(1)}) \tag{17}$$

$$U^{n+1} = \frac{1}{3}U^n + \frac{2}{3}U^{(2)} + \frac{2}{3}\Delta t L(U^{(2)}), \tag{18}$$

where U^{n+1} is the final value after advancing one time step from U^n.

For an explicit time integration scheme, the time step is constrained by the Courant-Friedrichs-Lewy (CFL) condition. The time step is determined as

$$dt = C\min_i\left(\frac{\Delta x^i}{\alpha^i}\right), \tag{19}$$

where C is a parameter called CFL number and α^i is the local largest speed of propagation of characteristics in the direction i whose explicit expression can be found in Donat et al. (1998).

3.2. *Reconstruction Method*

Generally speaking, there are two classes of spatially reconstruction schemes (see e.g. LeVeque 2002). One is reconstructing the unknown variables at the cell interfaces and then use exact or approximate Riemann solver to compute the fluxes. Another is direct flux reconstruction, in which we reconstruct the flux directly using the fluxes at cell center. To explore the coupling of different schemes with AMR as well as exploring which method is most suitable for a specific astrophysical problem, we have implemented several different schemes in both classes.

To reconstruct unknown variables, we have implemented piecewise linear method (PLM, Van Leer 1979), piecewise parabolic method (PPM, Colella & Woodward

1984, Martí & Müller 1996), the third-order convex essentially non-oscillatory scheme (CENO, Liu & Osher 1998). Those are used to reconstruct the primitive variables since reconstructing the conserved variables can produce unphysical values in SRHD. Furthermore, unphysical values of three-velocities may arise during the reconstruction especially for ultrarelativistic flows. So we either use $v^i W$ to do the reconstruction or we also reconstruct the Lorentz factor and use it to renormalize the reconstructed three-velocity when they are unphysical.

For direct flux reconstruction, we have implemented PLM and the third and fifth order WENO scheme of Jiang & Shu (1996). Direct flux reconstruction using WENO was first used to solve SRHD problems by Zhang & MacFadyen (2006). They showed that the fifth order WENO scheme works well with the third order Runge-Kutta time integration. In our implementation, we followed their description closely.

For the PLM and CENO schemes, we used a generalized minmod slope limiter (Kurganov & Tadmor 2000). For given v_{i-1}, v_i, v_{i+1}, $v_{i+1/2} = v_i + 0.5\mathrm{minmod}(\theta(v_i - v_{i-1}), 0.5(v_{i+1} - v_{i-1}), \theta(v_{i+1} - v_i))$, where $1 \leq \theta \leq 2$. For $\theta = 2$ it reduces to the monotonized central-difference limiter of Van Leer (1977). We found that this generalized minmod slope limiter behaves much better than a traditional minmod limiter (LeVeque 2002) especially for strong shear flows. In our calculation, $\theta = 1.5$ is used by default. For the PPM scheme, we used the parameters proposed by Martí & Müller (1996) for all the test problems. For WENO, we used the parameters suggested in the original paper of Jiang & Shu (1996).

3.3. *Riemann Solver*

In the first class of reconstruction methods, given the reconstructed left and right primitive variables at interfaces, the flux across each interface is calculated by solving the Riemann problem defined by those two states. An exact Riemann solver is quite expensive in SRHD (Martí & Müller 1994; Pons et al. 2000). Thus we have implemented several approximate Riemann solvers including HLL (Harten et al. 1983; Schneider et al. 1993; Kurganov et al. 2001), HLLC (Toro et al. 1994; Mignone & Bodo 2005), local Lax-Friedrichs (LLF, Kurganov & Tadmor 2000) and the modified Marquina flux (Aloy et al. 1999).

The HLLC scheme is an extension of the HLL solver developed by Toro et al. (1994) for Newtonian flow which is extended to two-dimensional relativistic flows by Mignone & Bodo (2005). The improvement of HLLC over HLL is restoring the full wave structure by constructing the two approximate states inside the Riemann fan. The two states can be found by the Rankine-Hugoniot conditions between those two states and the reconstructed states. With this modification, HLLC indeed behaves better than other Riemann solvers in some 1d (§ 5.1.7) and 2d (§ 5.2) test problems. But when we apply HLLC to three dimensional jet simulation, we found that HLLC suffers from the so called "carbuncle" artifact well-known in computational fluid dynamics literature (Quirk 1994). Then we have used HLLC to run many other two-dimensional test problems designed for detecting carbuncle artifact and we also saw the artifact. We found that the HLLC solver is unsuitable for many multidimensional problems. The discussion of those problems

will be presented elsewhere. In this work, we will only apply HLLC to two test problems showing that the HLLC solver has less smearing at contact discontinuities than other schemes.

Lucas-Serrano et al. (2004) has compared the HLL scheme, the LLF scheme and the modified Marquina flux formula. They found those three schemes give similar results for all their test problems. In our tests, we found similar results. But the modified Marquina flux formula is not as stable as HLL in problems with strong transverse flows and LLF is more diffusive than HLL. So in the following discussion we will only show the results using HLL in most of the tests if there is no difference among those three schemes.

In the following discussion, we will denote a specific hydro algorithm by X-Y where X is the flux formula and Y is the reconstruction scheme. For example, F-WENO5 denotes direct flux reconstruction using fifth order WENO. We used the third order Runge-Kutta method for all the tests in this work.

3.4. *Converting Conserved Variables to Primitive Variables*

Since primitive variables are needed in the reconstruction process, after every RK time step, we need to convert conserved variables to primitive variables. In SRHD, while conserved variables can be computed directly from primitive variables using Eqs. (8), (9) and (10), the inverse operation is not straightforward. One needs to solve a quartic equation for ideal gas EOS and a nonlinear equation for more complicated EOS. Normally an iteration method is used in SRHD code even for ideal gas EOS because computing the solution of quartic solution analytically is very expensive. Following Aloy et al. (1999), we have used a Newton-Raphson (NR) iteration to solve a nonlinear equation for pressure to recover primitive variables from conserved variables. Typically, the NR iteration needs only 2 to 3 steps to converge.

3.5. *Curvilinear coordinates*

We implemented cylindrical and spherical coordinates following the description of Zhang & MacFadyen (2006). This affects three parts of the code. Firstly, the geometric factors are incorporated into the flux when updating the conserved variables. Secondly, there will be geometric source terms. Thirdly, the flux correction in AMR (§ 4.4) is modified by geometric factors.

4. ADAPTIVE MESH REFINEMENT

4.1. *Overview*

Adaptive mesh refinement (AMR) was developed by Berger & Oliger (1984) and Berger & Colella (1989) to achieve high spatial and temporal resolution in regions where fixed grid resolution is insufficient. In the Berger & Colella structured AMR, a subgrid will be created in regions of its parent grid needing higher resolution. The hierarchy of grids is like a tree structure. Each grid is evolved as a separate initial boundary value problem. The whole grid hierarchy is evolved recursively.

renzo is built on top of the AMR framework of *enzo* (Bryan & Norman 1997a; O'Shea et al. 2004). *enzo*'s implementation of AMR follows closely the Berger & Colella paper and have been shown to be very efficient in

very high dynamical range cosmological simulations (see e.g. Abel et al. 2002). As an example, the pseudocode for second order Runge-Kutta method reads,

```
EvolveLevel  l
    SetBoundaryCondition
    while(t_l < t_{l-1})
        ComputeTimeStep  dt_l
        for every grid patch on this level
            Runge − Kutta  first  step :  Eq.(14)
                ComputeFlux
                    SweepX, Y, Z
                        ChooseHydroAlgorithm
                        SaveSubgridFlux
                UpdateConservedVariables
                ConservedToPrimitive
            UpdateTime :  t_l = t_l + dt_l
        SetBoundaryCondition(§ 4.2)
        for every grid patch on this level
            Runge − Kutta  second  step :  Eq.(15)
                ComputeFlux
                UpdateConservedVariables
                ConservedToPrimitive
        SetBoundaryCondition
        EvolveLevel  l + 1
        UpdateFromFinerGrid  (§ 4.4)
        FluxCorrection  (§ 4.4)
        RebuildHierarchy  for  level  l
```

The RebuildHierarchy function called at the end of every time step is at the heart of AMR. For reader's convenience, we also give the the pseudocode for this function implemented originally in *enzo*

```
RebuildHierarchy  for  level  l                    (20)
    for  i_level = l  to  MaximumLevel − 1
        for every grid on i_level
            FlagCellsForRefinement  (§ 4.3)
            CreateSubgrids
            AddLevel(i_level + 1)
        for every new subgrid
            InterpolateFieldValuesFromParent  (§ 4.2)
            CopyFromOldSubgrids
        LoadBalanceGrids
```

4.2. *Interpolation*

When a new subgrid is created, the initial values on that grid are obtained by interpolating spatially from its parent grid. In this case, we apply the conservative second order order interpolation routine provided by *enzo* to conserved variables. But in this process sometimes the interpolated values can violate the constraint $(\tau + D)^2 > S^2 + D^2$. If this happens, we will then use first order method for that subgrid.

Before the first Runge-Kutta step for a grid at level l (in the following discussion, we use the convention that top grid has level 0), we will need the boundary condition at time t_l, which can be get by interpolating from its parent grid. Then at the latter steps of Runge-Kutta schemes, we will need the boundary conditions at time $t_l + dt_l$. Since the variables of its parent grid has already been evolved to time $t_{l-1} + dt_{l-1}$, which is greater than time $t_l + dt_l$, we can obtain the boundary conditions at time $t_l + dt_l$ for a grid at level l by interpolating both temporally and spatially from its parent grid. There are two exceptions to this procedure. First, if a cell of fine grid abuts the box boundary, then we just use the specified boundary condition for that cell. Second, if a cell abuts another grid at the same level, then we just copy the value from that grid. Due to the above mentioned problem for interpolating conserved variables, when interpolating boundary values, we apply the second order interpolation to primitive variables. Since for ultrarelativistic flows spatially interpolating three-velocity can lead to unphysical values, so we also interpolate the Lorentz factor and then use it to renormalize the interpolated three-velocity.

4.3. *Refinement Criteria*

In the test problems discussed in section 5, we mainly used two general purpose refinement criteria that have been widely used in AMR code.

In the first one, we compute the slope

$$S_i = \frac{|u_{i+1} - u_{i-1}|}{\max(|u_i|, \epsilon)}, \tag{21}$$

where u_i is typically density, pressure and velocities, ϵ is a small number typically taken to be 10^{-10}. When S_i is larger than a minimum slope, typically 1, a cell will be flagged for refinement.

In the second one, for every cell we compute

$$E_i = \frac{|u_{i+2} - 2u_i + u_{i-2}|}{|u_{i+2} - u_i| + |u_i - u_{i-2}| + \epsilon(|u_{i+2}| + 2|u_i| + |u_{i-2}|)}, \tag{22}$$

which is the ratio of the second and first derivatives with a safety factor in the denominator. Unless otherwise stated, we use $\epsilon = 0.01$. When E_i is larger than a critical value E_{ref}, a cell will be flagged for refinement. Typically we use $E_{ref} = 0.8$.

To fully exploit the power of AMR, it is desirable to design more specific refinement criterion that is most efficient for a specific astrophysical problem. We will discuss more effective refinement strategies elsewhere.

4.4. *Flux Correction*

When a cell is overlayed by a finer level grid, then the coarse grid value is just the conservative average of the fine grid values. On the other hand, when a cell abuts a fine grid interface but is not itself covered by any fine grid, we will do flux correction for that cell, i.e. we will use the fine grid flux to replace the coarser grid flux in the interface abutting the fine grid.(see Berger & Colella 1989 for more detailed description of flux correction). For this purpose, note that the second order Runge-Kutta method can be rewritten as

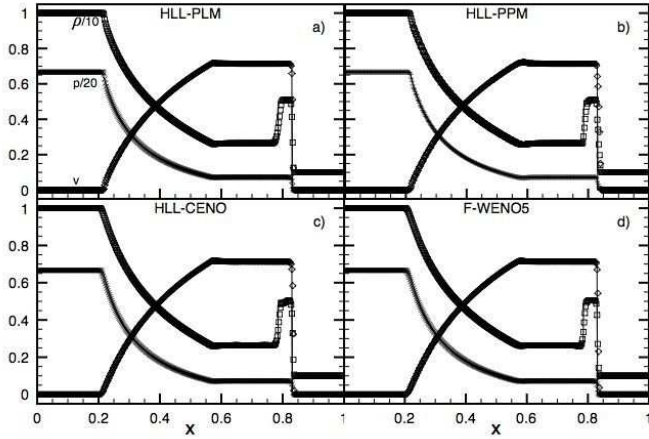$$U^{n+1} = U^n + \frac{1}{2}\Delta t L(U^n) + \frac{1}{2}\Delta t L(U^{(1)}), \tag{23}$$

FIG. 1.— Relativistic blast wave I at $t = 0.4$ with uniform resolution $N = 400$ for (a) HLL-PLM, (b) HLL-PPM, (c) HLL-CENO and (d) F-WENO5. Numerical profiles of density (squares), pressure (cross signs) and velocity (diamonds) are shown as well as the analytical solution (solid lines). The CFL number used is 0.5.

and the third order Runge-Kutta method can be rewritten as

$$U^{n+1} = U^n + \frac{1}{6}\Delta t L(U^n) + \frac{1}{6}\Delta t L(U^{(1)}) + \frac{2}{3}\Delta t L(U^{(2)}).$$
(24)

Thus for example, when we do flux correction in the x-direction for interface $i+1/2$, we will use $F^x_{i+1/2}(U^n)/2 + F^x_{i+1/2}(U^{(1)})/2$ and $F^x_{i+1/2}(U^n)/6 + F^x_{i+1/2}(U^{(1)})/6 + 2F^x_{i+1/2}(U^{(2)})/3$ to correct the coarser grid conserved variables for the second and third order Runge-Kutta method, respectively.

4.5. Parallelism

renzo uses the enzo parallel framework which uses dynamically load balancing using the Message Passing Interface (MPI) library. At run time, the code will move grids among processors according to the current load of every processor to achieve a balanced distribution of computational load among processors. The computational load of a processor is defined as the total number of active cells on that processor and level.

5. CODE TESTS

5.1. One Dimensional Test

Relativistic Riemann problems have analytical solutions (Pons et al. 2000), thus they are ideal for tesing SRHD codes. In the following discussion, subscript L and R refer to the left and right initial states, respectively. The initial discontinuity is always at $x = 0.5$. We will report the error between numerical solutions and analytical solutions using L_1 norm defined as $L_1 = \Sigma_i |u_i - u(x^i)|\Delta x^i$ where u_i is the numerical solution, $u(x^i)$ is the analytical solution and Δx^i is the cell width.

5.1.1. Relativistic Blast Wave I

This test and the following one are fairly standard and all modern SRHD codes can match the analytical solution quite well (see Martí & Müller 2003 for a summary of different codes' performance on those two tests).

The initial left and right states for this problem are $p_L = 13.33, \rho_L = 10.0, v_L = 0.0$ and $p_R = 10^{-6}$,
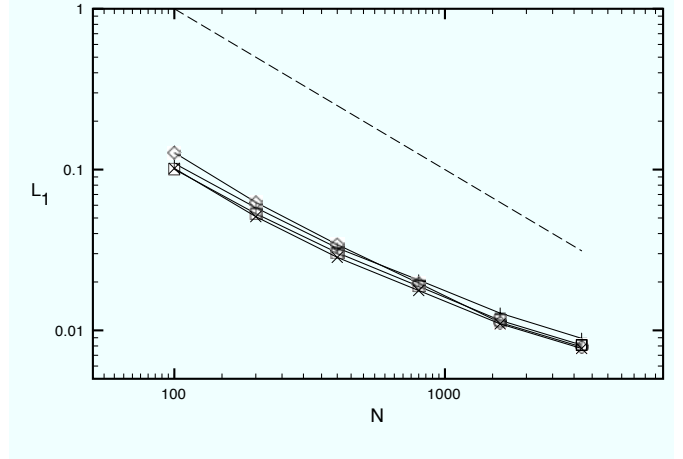

FIG. 2.— L1 errors in rest mass density for the relativistic blast wave I problem for six different uniform grid resolutions. The symbols denote HLL-PLM (plus signs), HLL-PPM (diamonds), HLL-CENO (squares) and F-WENO5 (cross signs). The dashed line indicates first order of global convergence.
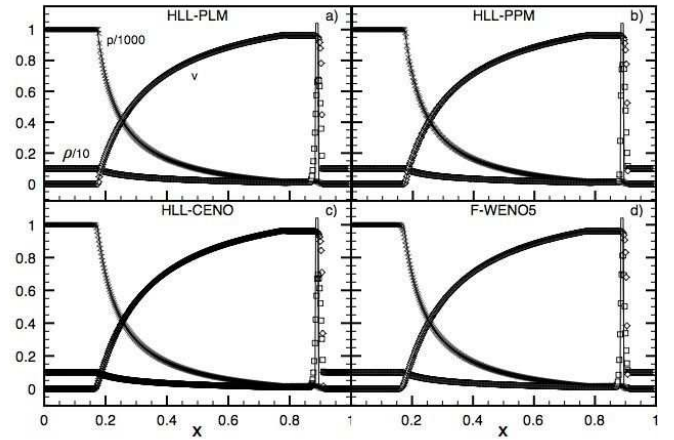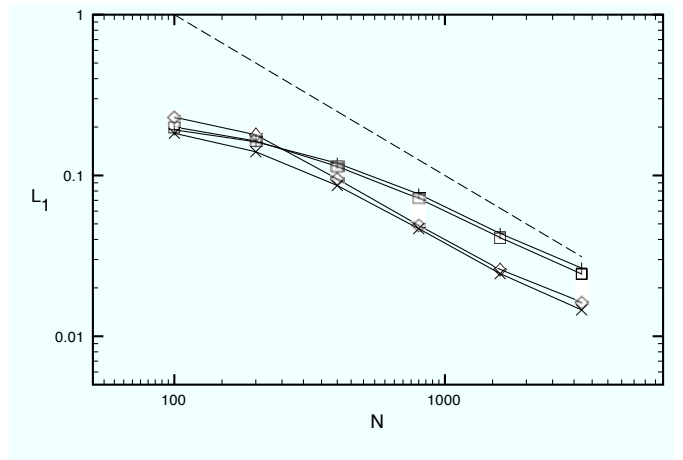

FIG. 3.— Relativistic blast wave II at $t = 0.4$ with uniform resolution $N = 400$ for (a) HLL-PLM, (b) HLL-PPM, (c) HLL-CENO and (d) F-WENO5. Numerical profiles of density (squares), pressure (cross signs) and velocity (diamonds) are shown as well as the analytical solution (solid lines). The CFL number used is 0.5.

FIG. 4.— L1 errors in rest mass density for the relativistic blast wave II problem for six different uniform grid resolutions. The symbols denote HLL-PLM (plus signs), HLL-PPM (diamonds), HLL-CENO (squares) and F-WENO5 (cross signs). The dashed line indicates first order of global convergence.
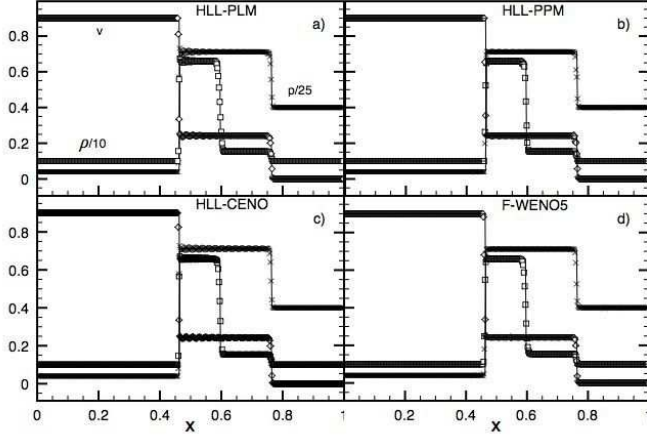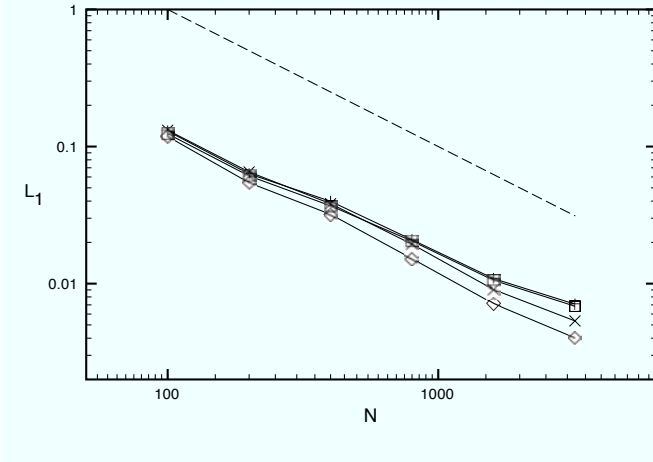
FIG. 5.— Planar jet problem at $t = 0.4$ with uniform resolution $N = 400$ for (a) HLL-PLM, (b) HLL-PPM, (c) HLL-CENO and (d) F-WENO5. Numerical profiles of density (squares), pressure (cross signs) and velocity (diamonds) are shown as well as the analytical solution (solid lines). The CFL number used is 0.5.
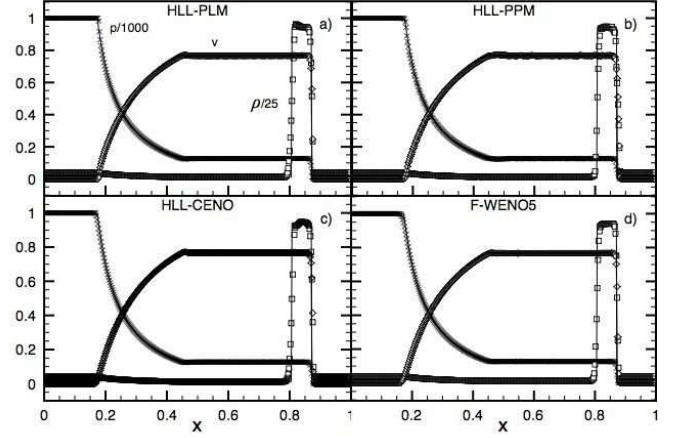

FIG. 7.— Blast wave with transverse velocity problem I at $t = 0.4$ with uniform resolution $N = 400$ for (a) HLL-PLM, (b) HLL-PPM, (c) HLL-CENO and (d) F-WENO5. Numerical profiles of density (squares), pressure (cross signs) and velocity (diamonds) are shown as well as the analytical solution (solid lines). The CFL number used is 0.5.
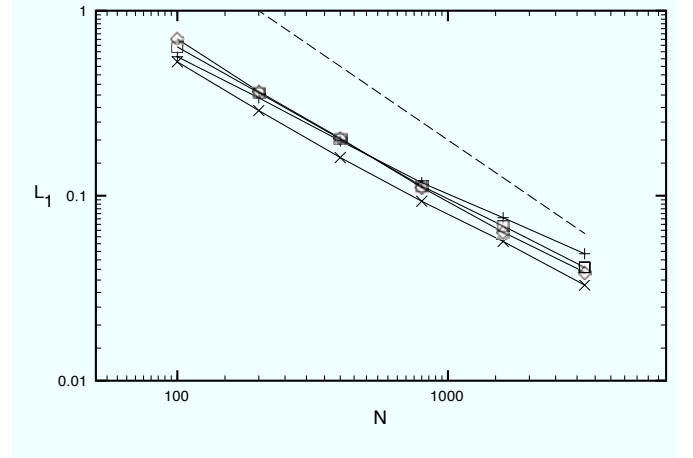

FIG. 6.— L1 errors in rest mass density for the planar jet problem for six different uniform grid resolutions. The symbols denote HLL-PLM (plus signs), HLL-PPM (diamonds), HLL-CENO (squares) and F-WENO5 (cross signs). The dashed line indicates first order of global convergence.

$\rho_R = 1.0$, $v_R = 0.0$. The gas is assumed to be ideal with an adiabatic index $\Gamma = 5/3$. The initial discontinuity gives rise to a transonic rarefaction wave propagating left, a shock wave propagating right and a contact discontinuity in between. This problem is only mildly relativistic with a post-shock velocity 0.72 and shock velocity 0.83. The results using four hydro solvers are shown in Fig. 1. The CFL number used is 0.5. The L_1 errors are shown in Fig. 2, from which we can see the four schemes behave essentially identically for this problem. The order of global convergence rate is about 1 for all four schemes, which is consistent with the fact there are discontinuities in the problem.

5.1.2. *Relativistic Blast Wave II*

The initial left and right states for this problem are $p_L = 1000.0, \rho_L = 1.0, v_L = 0.0$ and $p_R = 10^{-2}$, $\rho_R = 1.0$, $v_R = 0.0$. The gas is assumed to be ideal with an adiabatic index $\Gamma = 5/3$. This test is more relativistic than the previous one. While the wave structure is the same, the thermodynamically relativistic initial left state

FIG. 8.— L1 errors in rest mass density for the blast wave with transverse velocity problem I for six different uniform grid resolutions. The symbols denote HLL-PLM (plus signs), HLL-PPM (diamonds), HLL-CENO (squares) and F-WENO5 (cross signs). The dashed line indicates first order of global convergence.

gives rise to a relativistic shock propagating at a Lorentz factor $W \approx 6$ and a very thin dense shell behind the shock with width ≈ 0.01056 at $t = 0.4$. The CFL number used is 0.5. The results using four hydro algorithms are shown in Fig. 3. The L_1 errors are shown in Fig. 4. We can see that for this problem PPM and WENO have smaller L_1 error than PLM and CENO. This is due to their better resolution of the thin shell.

5.1.3. *Planar Jet Propagation*

The initial left and right states for this test are $p_L = 1.0, \rho_L = 1.0, v_L = 0.9$ and $p_R = 10.0$, $\rho_R = 1.0$, $v_R = 0.0$. The gas is assumed to be ideal with an adiabatic index $\Gamma = 4/3$. This test mimics the interaction of a planar jet head with the ambient medium. The decay of the initial discontinuity gives rise to a strong reverse shock propagating to the left, a forward shock propagating to the right and a contact discontinuity in between. The results are shown in Fig. 5. The CFL number is 0.5. The L_1 errors are shown in Fig. 6. As can be
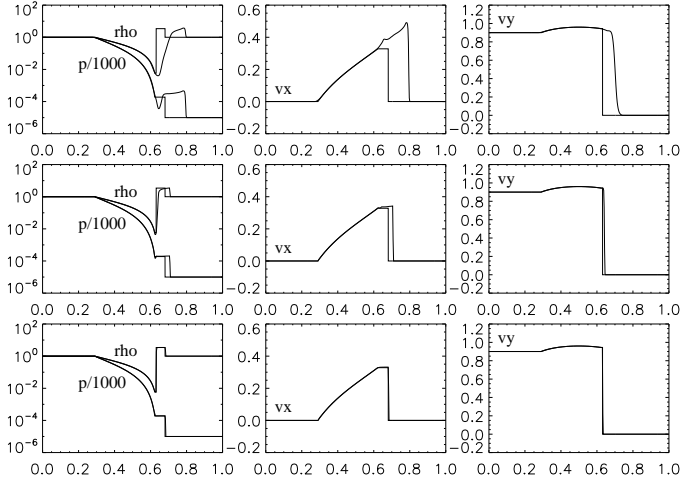
FIG. 9.— Blast wave with transverse velocity problem II at $t = 0.4$ with uniform resolution $N = 400$ (top), 4 refinement levels with a refinement factor of 2 (middle, equivalent resolution 6400) and 3 refinement levels with a refinement factor of 4 (bottom, equivalent resolution 25600). The hydro solver used is HLL-PLM. Thick lines are numerical solution while thin lines are analytical solutions. The CFL number used is 0.4
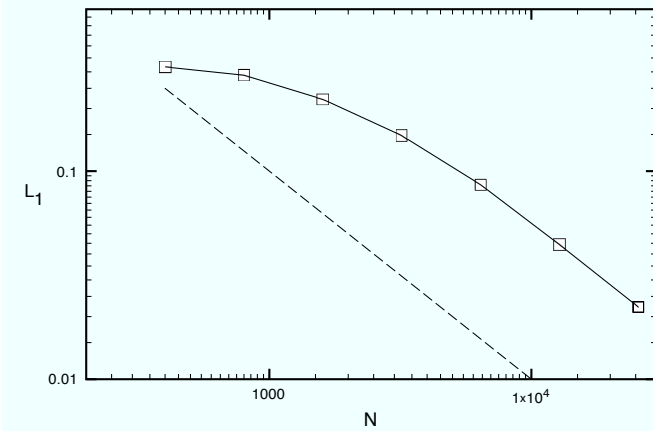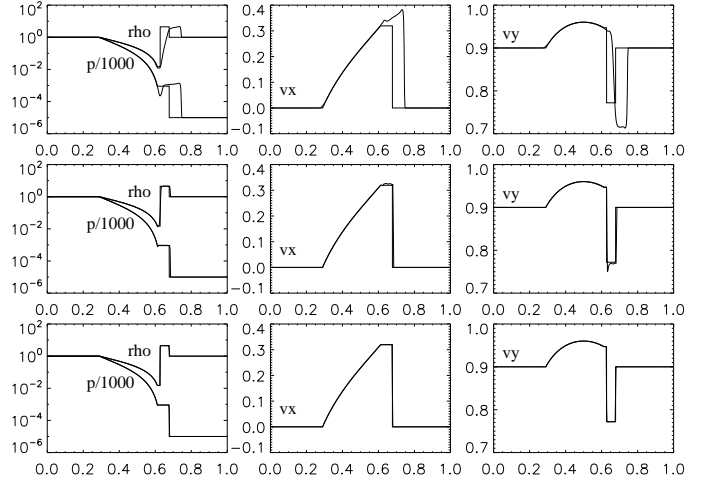

FIG. 11.— Blast wave with transverse velocity problem III at $t = 0.4$ with uniform resolution $N = 400$ (top), 4 refinement levels with a refinement factor of 2 (middle, equivalent resolution 6400) and 4 refinement levels with a refinement factor of 3 (bottom, equivalent resolution 25600). The hydro solver used is HLL-PLM. Thick lines are numerical solutions while thin lines are analytical solutions. The CFL number used is 0.5
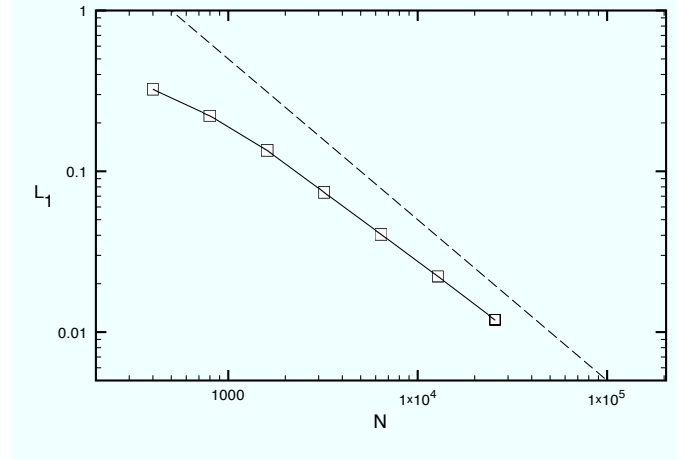

FIG. 10.— L1 errors in rest mass density for the blast wave with transverse velocity problem II for seven different equivalent grid resolutions using AMR. The solid lines with square signs are for HLL-PLM. The dashed line indicates first order of global convergence.

FIG. 12.— L1 errors in rest mass density for the blast wave with transverse velocity problem III for seven different equivalent grid resolutions using AMR. The solid lines with square signs are HLL-PLM. The dashed line indicates first order of global convergence.

seen in Figs. 5 & 6, for this problem PPM and WENO behave better than PLM and CENO: there is almost no oscillation behind the reverse shock and they capture the contact discontinuity with fewer cells. Especially PPM captures the contact discontinuity with only 4 cells and has the smallest L_1 error.

5.1.4. *Blast Wave with Transverse Velocity I*

For this problem and the following two, we will consider non-zero transverse velocities in the initial states. The initial state is identical to blast wave problem II except the presence of transverse velocities. Those problems were first discussed analytically by Pons et al. (2000). Since then various groups have shown that when transverse velocities are non-zero, in some cases those problems become very difficult to solve numerically unless very high spatial resolution is used (Mignone et al. 2005; Zhang & MacFadyen 2006; Morsony et al. 2006).

In realistic astrophysical phenomena transverse velocities are usually very important (see e.g. Aloy & Rezzolla 2006), thus solving those problems accurately is of great importance.

As an easy first case, we will consider non-zero transverse velocity only in the low pressure region. The initial left and right states are $p_L = 1000.0$, $\rho_L = 1.0$, $v_{xL} = 0.0$, $v_{yL} = 0.0$ and $p_R = 10^{-2}$, $\rho_R = 1.0$, $v_{xR} = 0.0$, $v_{yR} = 0.99$. The gas is assumed to be ideal with an adiabatic index $\Gamma = 5/3$. The results are shown in Fig. 7. The CFL number is 0.5. The L_1 errors are shown in Fig. 8. We can see that all four hydro algorithms behaves quite well and similarly, except that PLM and CENO shows some small oscillation around the contact discontinuity.

5.1.5. *Blast Wave with Transverse Velocity II*

Next, we will consider non-zero transverse velocity in the high pressure region. In this case, the problem be-

TABLE 1
Equivalent resolution and the actual cell number used in Blast Wave problems with Transverse Velocity II (BT II) and III (BT III).

Equivalent Resolution	BT II	BT III
400	400	400
800	448	421
1600	455	442
3200	470	468
6400	501	473
12800	518	476
25600	562	520

comes difficult to solve numerically (Mignone et al. 2005; Zhang & MacFadyen 2006). The initial left and right states for this problem are $p_L = 1000.0, \rho_L = 1.0, v_{xL} = 0.0, v_{yL} = 0.9$ and $p_R = 10^{-2}, \rho_R = 1.0, v_{xR} = 0.0, v_{yR} = 0.0$. The gas is assumed to be ideal with an adiabatic index $\Gamma = 5/3$. The high pressure region is connected to the intermediate state by a rarefaction wave. Since the initial normal velocity in the high pressure region is zero, the slope of the adiabat increases rapidly with transverse velocity, thus a large initial transverse velocity will lead to a small intermediate pressure and a small mass flux.

The results using a uniform grid and two AMR runs are shown in Fig. 9. The hydro solver used for this figure is HLL-PLM. The CFL number is 0.4. The L_1 error are shown in Fig. 10. It can be seen that for the run with 400 uniform grid cells, the numerical solution is very inaccurate, as previously found by Mignone et al. (2005). This is mainly due to the poor capture of the contact discontinuity. We have tried to run this problem with various algorithms but looks like currently increasing resolution was the only way to get the correct solution.

5.1.6. *Blast Wave with Transverse Velocity III*

Now we introduce transverse velocity in both region. The initial left and right states for this problem are $p_L = 1000.0, \rho_L = 1.0, v_{xL} = 0.0, v_{yL} = 0.9$ and $p_R = 10^{-2}, \rho_R = 1.0, v_{xR} = 0.0, v_{yR} = 0.9$. The gas is assumed to be ideal with an adiabatic index $\Gamma = 5/3$. This problem is more difficult than the previous one due to the formation of an extremely thin shell between the rarefaction wave tail and the contact discontinuity (Zhang & MacFadyen 2006).

The results with a uniform grid and two AMR runs are shown in Fig. 11. The hydro solver used for this run is HLL-PLM. The CFL number used is 0.5. The L_1 errors are shown in Fig. 12.

Table 1 shows the equivalent resolution and the actual number of cells used for this and the previous tests. It can be seen for the highest resolution calculation our code uses about four hundred times less grid cells than the corresponding uniform grid calculation. Thus AMR allows us to achieve very high resolution while reducing computational cost significantly.

5.1.7. *Jet-Cocoon interaction*

For this test we set up a one-dimensional Riemann problem that mimics the interaction of jet with an over-pressured cocoon. The initial left and right states for this problem are $p_L = 0.00017, \rho_L = 0.01, v_{xL} = 0, v_{yL} = 0.99$ and $p_R = 0.017, \rho_R = 0.1, v_{xR} = 0, v_{yR} = 0$. The
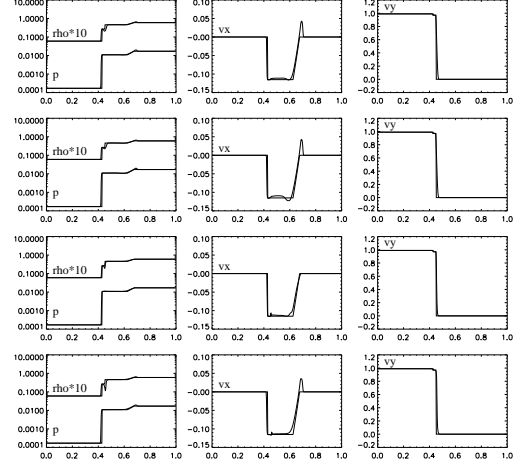

Fig. 13.— Jet-cocoon interaction problem at $t = 0.4$ for (from top to bottom): HLL-PLM, LLF-PLM, HLLC-PLM and F-PLM. Thick lines are numerical solution while thin lines are analytical solutions. The grid resolution is uniform $N = 400$. The CFL number is 0.5.

gas is assumed to be ideal with $\Gamma = 5/3$. Those values mimic the conditions of the jet-cocoon boundary in model C2 of Marti et al. (1997). The result using four different Riemann solver with PLM on uniform grid are shown in Fig. 13. It can be seen that solutions use HLL, LLF and direct flux reconstruction have large positive fluctuations in the normal velocity at the rarefaction wave. It is interesting to note that only HLLC does not suffer from this shortcoming which is probably due to the ability of HLLC to resolve contact discontinuity compared to the other Riemann solvers in the code. If those fluctuations also happen in higher dimensional jet simulation, then one would expect that the normal velocity fluctuation seen in this test would lead to a artificially more extended cocoon.

In Fig. 14 the result of using HLL-PLM and HLLC-PLM with AMR is shown. It can been seen that the fluctuation in the HLL scheme becomes smaller with higher resolution. Fig. 15 shows the L_1 error for those two schemes with different levels of refinement.

5.2. *Two Dimensional Test: Shock Tube*

To test the code in higher dimension, we first study the two-dimensional shock tube problem suggested by Del Zanna & Bucciantini (2002) and latter also used by various groups (see e.g. Zhang & MacFadyen 2006, Mignone & Bodo 2005a, Lucas-Serrano et al. 2004). This test is done in a two-dimensional Cartesian box divided into four equal-area-constant states:

$$(\rho, v_x, v_y, p)^{NE} = (0.1, 0, 0, 0.01), \quad (25)$$
$$(\rho, v_x, v_y, p)^{NW} = (0.1, 0.99, 0, 1),$$
$$(\rho, v_x, v_y, p)^{SW} = (0.5, 0, 0, 1),$$
$$(\rho, v_x, v_y, p)^{SE} = (0.1, 0, 0.99, 1),$$

where NE means northeast corner and so on. The grid is uniform 400×400. The gas is assumed to be ideal with an adiabatic index $\Gamma = 5/3$. We use outflow boundary conditions in all four directions and the CFL number is 0.5.
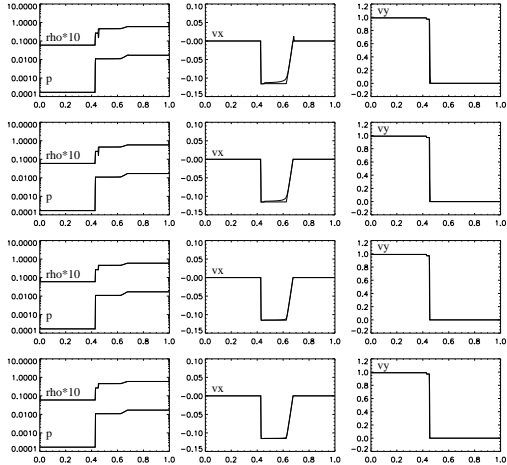
FIG. 14.— Jet-cocoon interaction problem at $t = 0.4$ for HLL-PLM and HLLC-PLM. The top two are HLL-PLM and HLLC-PLM with 4 refinement levels and a refinement factor of 2 (equivalent resolution 6400). The bottom two are HLL-PLM and HLLC-PLM with 4 refinement levels and a refinement factor of 4 (equivalent resolution 102400). Thick lines are numerical solutions while thin lines are analytical solutions. The CFL number is 0.5.
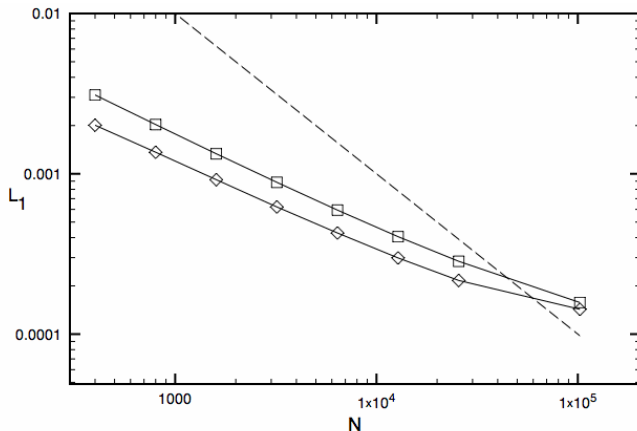

FIG. 15.— L_1 error for the jet-cocoon interaction problem for eight different grid resolutions using AMR. The square signs are for HLL-PLM while the diamonds are HLLC-PLM. The dashed line indicates first order of global convergence.

The results are shown in Fig. 16 for four schemes. This problem does not have analytical solutions to compare with, but comparing our result with other groups' result shows good agreement. The cross in the lower left corners of (a) HLL-PLM and (d) F-WENO is a numerical artifact due to the inability to maintain a contact discontinuity perfectly, which are absent in the results using the HLLC solver (c). This agreed with the result of Mignone & Bodo (2005) that the HLLC solver behaves better in this problem than other Riemann solvers due to its ability of resolving contact discontinuity.

5.3. Three Dimensional Test

5.3.1. Relativistic Spherical Shock Reflection

We first study a test problem with uniform grid in Cartesian coordinate that has been used by several groups to test the symmetric properties of a three-dimensional SRHD code (Aloy et al. 1999;

Mignone et al. 2005). The initial setup of this test consists of a cold spherical inflow with initially constant density ρ_0 and constant velocity v_1 colliding at the box center. This problem is run using three-dimensional Cartesian coordinates so it allows one to evaluate the symmetry properties of the code (Marti et al. 1997; Aloy et al. 1999; Mignone et al. 2005). When gas collide at the center, a reflection shock will form. Behind the shock, the kinetic energy will be converted completely into internal energy. Thus the downstream velocity v_2 is zero and the specific internal energy is given by the upstream specific kinetic energy

$$\epsilon_2 = W_1 - 1. \tag{26}$$

Using the shock jump condition, the compression ratio ρ_2/ρ_1 and the shock velocity can be found to be

$$\frac{\rho_2}{\rho_1} = \frac{\Gamma + 1}{\Gamma - 1} + \frac{\Gamma}{\Gamma - 1}\epsilon_2 \tag{27}$$

$$V_s = \frac{(\Gamma - 1)W_1|v_1|}{W_1 + 1}. \tag{28}$$

In the unshocked region ($r > V_s t$), the gas flow will develop a self-similar density distribution,

$$\rho_1 = \left(1 + \frac{v_1 t}{r}\right)^2 \rho_0. \tag{29}$$

The initial state are $p_1 = 7 \times 10^{-6}, \rho_0 = 1, v_1 = -0.9$. We chose a small value for pressure because a grid-based code cannot handle zero pressure. A CFL number 0.1 is used for this problem, as other groups (Aloy et al. 1999). We chose to use LLF-PLM for this problem because this turns out to be the most stable solver for this problem. Fig. 17 shows the one-dimensional cut though axis and diagonal direction and Fig. 18 shows a contour through $z = 0.5$ plane, both at $t = 0.4$. It can be seen from those plots that our code keeps the original spherical symmetry quite well. Since in a Cartesian box the simple outflow boundary condition is inconsistent with the initial spherical inflow setup, we evolve this problem only to $t = 0.4$, at which point all the mass in the original box has just entered the shocked region (see Fig. 17). After that time, the evolution would be affected by the unphysical boundary condition.

5.3.2. Relativistic Blast Wave I

In this test, we study a spherical blast wave in three-dimensional Cartesian coordinates. There is no analytical solution for this problem. Thus for the sake of comparison, we set up the same problem as other groups (Del Zanna & Bucciantini 2002; Zhang & MacFadyen 2006). The center of the blast wave source is located at the corner $(0, 0, 0)$ of the box. The initial conditions are

$$(\rho, v_r, p) = (1, 0, 1000) \ \text{if} \ \ r \leq 0.4, \tag{30}$$
$$(\rho, v_r, p) = (1, 0, 1) \ \text{if} \ \ r > 0.4,$$

where r is the distance to the center $(0, 0, 0)$.

An ideal gas with an adiabatic index of $\Gamma = 5/3$ is assumed. The left boundaries at x, y, z directions are reflecting while others are outflow. We use a top grid of 128^3 zones with two more levels of refinement and a refinement factor of 2 for this calculation (equivalent
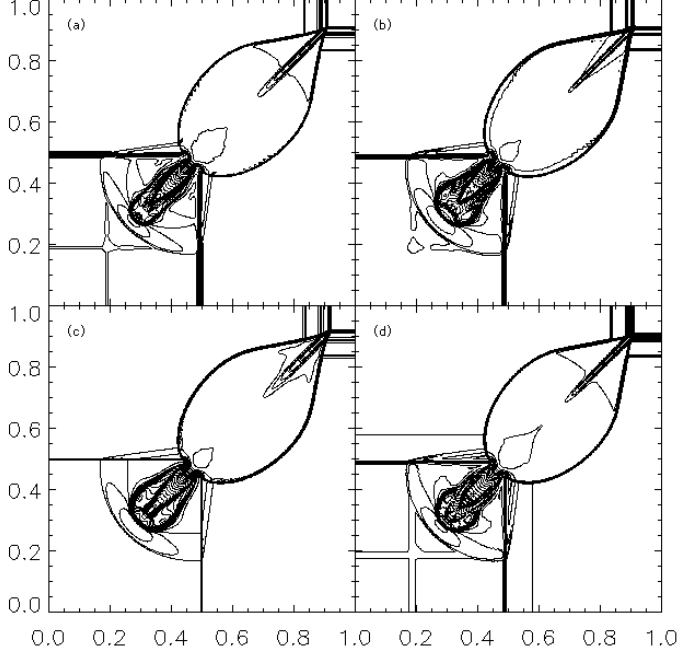
FIG. 16.— Shock tube problem at $t = 0.4$ for (a) HLL-PLM, (b) HLL-PPM, (c) HLLC-PLM and (d) F-WENO5. Thirty equally spaced contours of the logarithm of density are plotted. The CFL number is 0.3.
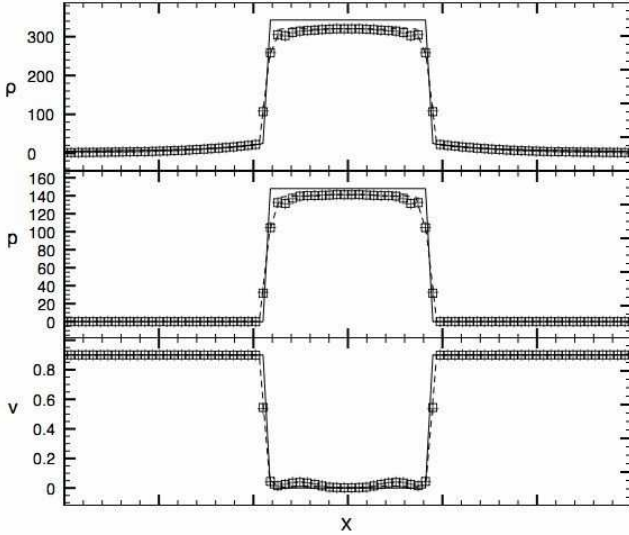

FIG. 18.— Density contour through $z = 0.5$ of of the relativistic spherical shock reflection problem at $t = 0.4$. It can be seen that the symmetry of the initial condition is preserved rather well up to this time. After this time, the unphysical boundary condition will begin to affect the subsequent evolution.

FIG. 17.— One-dimensional cut of the relativistic spherical shock reflection problem at $t = 0.4$ for density (top), pressure (middle) and radial velocity (bottom). The solid line is the analytical solution. Square signs, plus signs and dashed lines are cut though x axis, y axis and diagonal direction, respectively. The resolution is a uniform grid with 128^3 zones. LLF-PLM are used with a CFL number of 0.1. It can be seen that the fluctuations in density and pressure at the sphere center present in many previous codes are absent in our results.

FIG. 19.— One-dimensional cut of the three-dimensional blast wave problem I at $t = 0.4$ for density (top), pressure (middle) and velocity (bottom). The triangle signs and cross signs are cuts along the x axis and diagonal direction, respectively. The solid line is a one-dimensional simulation run using spherical coordinates with 4000 uniform zones. F-PLM is used for this calculation. A top grid of 128^3 zones with two levels of refinement and a refinement factor of 2 is used. The CFL number is 0.1.

resolution 512^3). F-PLM is used for the result shown and the CFL number is 0.1.

The results are shown in Fig. 19 where it shows the cut along x-axis and diagonal direction. For comparison, we run a high resolution one-dimensional simulation using spherical coordinates. The three-dimensional run in Cartesian coordinates agrees with the one-dimensional high resolution run. Furthermore, it can be seen that the
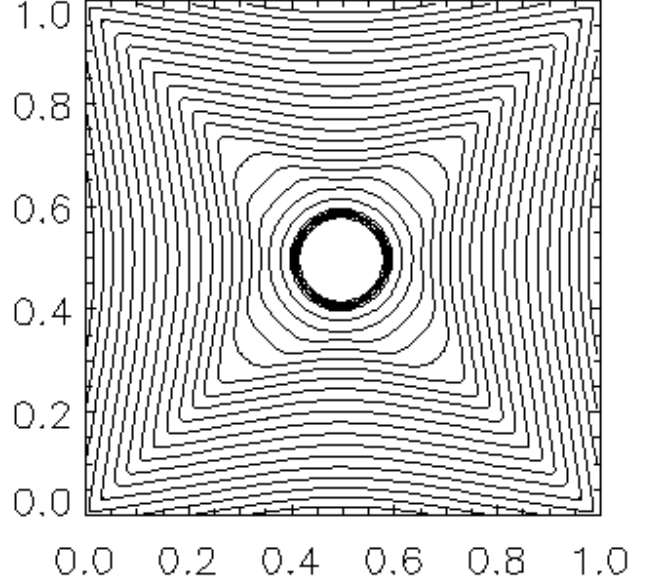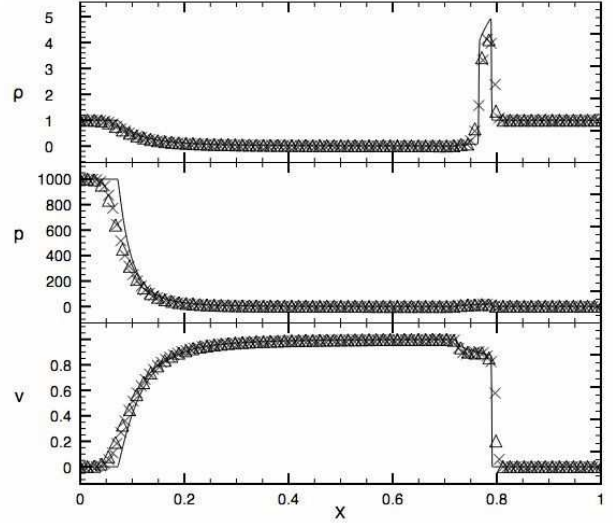
spherical symmetry of the initial condition is preserved rather well in the three-dimensional Cartesian run.

5.3.3. Relativistic Blast Wave II

Finally we study another blast wave problem for which the center of the blast wave source is located at the box center. This problem also does not have analytical solution but it has been studied by (Hughes et al. 2002) so our result can be compared to theirs. The initial condi-
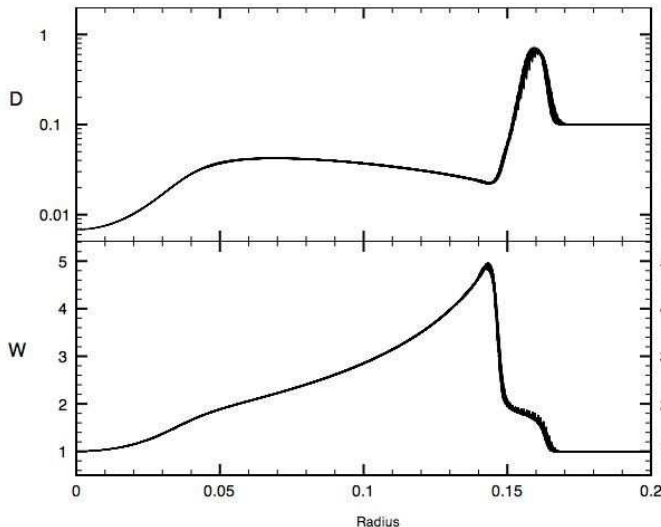
FIG. 20.— Three-dimensional blast wave problem II at $t = 0.12$. All points in a slice at $y = 0.5$ are plotted as a function of the distance to the center $(0.5, 0.5, 0.5)$. The upper panel shows the laboratory density D and the lower panel shows the Lorentz factor W. HLL-PLM is used for this calculation. A top grid of 64^3 zones with four levels of refinement and a refinement factor of 2 is used. The CFL number is 0.5.

tions are

$$(\rho, v_r, p) = (1, 0, 10^4) \quad \text{if} \quad r \leq 0.05, \qquad (31)$$
$$(\rho, v_r, p) = (0.1, 0, 10) \quad \text{if} \quad r > 0.05.$$

An ideal gas EOS with an adiabatic index of $\Gamma = 4/3$ is used. We stop the run at $t = 0.12$, roughly the same ending time of Hughes et al. (2002). A top grid of 64^3 zones with four levels of refinement and a refinement factor of two is used (equivalent resolution 1024^3). Thus our resolution is roughly 1.5 times of Hughes et al. (2002). We used HLL-PLM and a CFL number of 0.5 for this calculation.

Fig. 20 plots the numerical solution for all cells centered on the highest level in the two dimensional slice at $y = 0.5$ at $t = 0.12$ as a function of radius from the center (0.5,0.5,0.5). The position and amplitude of the high density shell agrees with the calculation of Hughes et al. (2002). And it can be seen that the spherical symmetry is preserved rather well in our code.

6. AN ASTROPHYSICAL APPLICATION: RELATIVISTIC SUPERSONIC JET PROPAGATION

In this section, we study a relativistic supersonic jet in three dimensions. We set up the problem using the same parameters as model C2 of (Marti et al. 1997). This model has also been studied in two dimensions by Zhang & MacFadyen (2006) and in three dimensions by Aloy et al. (1999). The jet parameters are $\rho_b = 0.01$, $v_b = 0.99$ and $r_b = 0.02$. The jet has a classical Mach number $M_b = v_b/c_s = 6$ so the pressure is $p_b = 0.000170305$. The parameters for the medium are $\rho_m = 1.0$, $v_m = 0$ and $p_m = p_b$. The EOS is assumed to be ideal with $\Gamma = 5/3$. The jet is injected from the low-z boundary centered at $(0.5, 0.5, 0)$ with radius r_b. Outflow boundary conditions are used at other part of the boundary.

Figure 21 shows the result at $t = 60r_b/c$ for the three runs: HLL-PPM with three levels of refinement

(HLL-PPM-l3), HLL-PLM with three levels of refinement (HLL-PLM-l3) and HLL-PLM with four levels of refinement (HLL-PLM-l4). The top grid resolution is 64^3 zones. Thus the first two runs have an equivalent resolution of 512^3 zones while the last one has 1024^3 zones. For the first two, turbulence in cocoon is not fully developed so the cocoon is still symmetric even in 3d. The HLL-PPM-l3 run has slightly more turbulent cocoon due to the higher spatial reconstruction order of PPM. Thus the HLL-PPM-l3 jet propagates slightly slower than the HLL-PLM-l3 jet. On the other hand, for the HLL-PLM-l4 jet, the resolution is 20 cells per beam radius, comparable to the resolution used in the two-dimensional study by Marti et al. (1997). The cocoon turbulence is much more developed in this case, just like in the 2d case (Marti et al. 1997). Consequently, the HLL-PLM-l4 jet propagates slower than the two lower resolution ones. Furthermore, the HLL-PLM-l4 case does not show axisymmetry because instability quickly develops in the lateral motion and consequently lateral motion also becomes turbulent.

7. CONCLUSIONS AND DISCUSSIONS

In this paper, we have described a new code that solves the special relativistic hydrodynamics equations with both spatially and temporally adaptive mesh refinement. It includes direct flux reconstruction and four approximate Riemann solvers including HLLC, HLL, LLF and modified Marquina flux formula. It contains several reconstruction routines including PLM, PPM, third order CENO, and third and fifth order WENO schemes. The highly modular code structure make it easy to include more physics modules and new algorithms.

From our test problems, it is clear that relativistic flow problems are more difficult than the Newtonian case. One of the reason is that in the presence of utrarelativistic speed, nonlinear structures such as shocked shells are typically much thinner and thus requires the use of very high spatial resolution. SRHD problems become difficult to solve accurately when significant transverse velocities are present in the problem as we have shown using several one dimensional problems. One reason for this difficulty is that in SRHD velocity components are coupled nonlinearly via the Lorentz factor. In studying astrophysical jet problems, we have demonstrated the need of both high resolution achievable only through AMR and careful choice of hydrodynamic algorithms.

To study astrophysical problems, we will implement more physics modules including gravity, advection of nuclear species, physical EOS, neutrino physics and magnetohydrodynamics. We will discuss those modules and their tests in more detail in future publications.
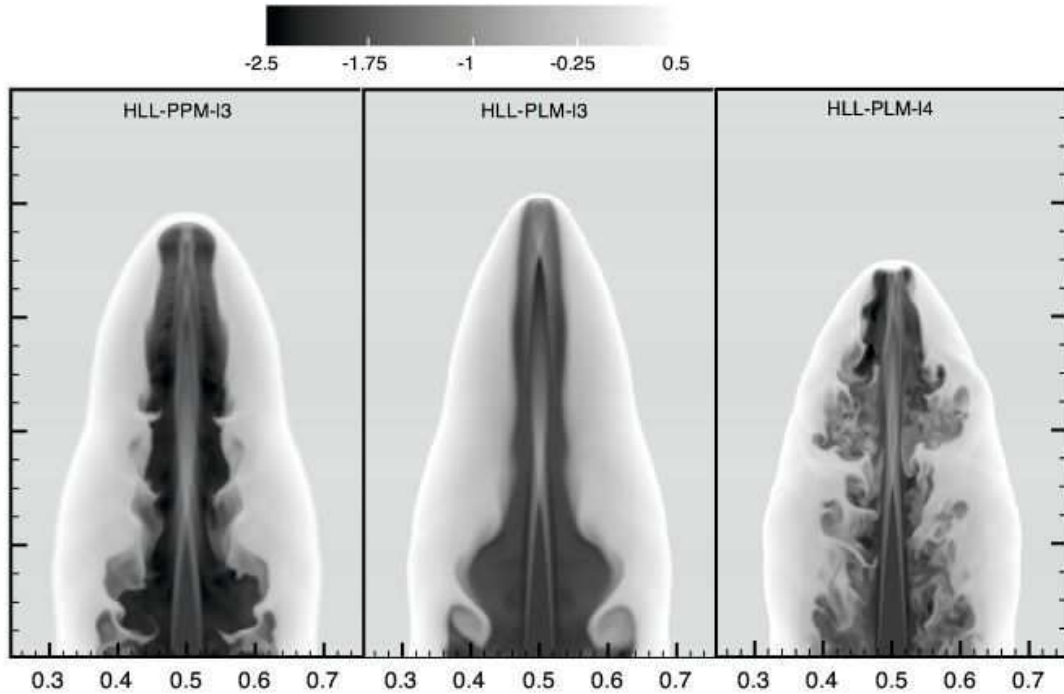
FIG. 21.— Density slice through $y = 0.5$ for three dimensional relativistic jet at $t=60r_b/c$ for HLL-PPM with three levels of refinement (left), HLL-PLM with three levels of refinement (middle) and HLL-PLM with four levels of refinement (right). The top grid resolution is 64^3 zones and a refinement factor of 2 is used. Thus the left and middle panels have an equivalent resolution of 512^3 zones while the right one has 1024^3 zones. The CFL number is 0.4.

REFERENCES

Abel, T., Bryan, G. & Norman, M., 2002, Science, 295, 93
Aloy, M.-A., Ibáñez, J. M., Martí, J. M. & Müller, E. 1999, ApJS, 122, 151
Aloy, M. A., & Rezzolla, L. 2006, ApJ, 640, L115
Anile, A. M., 1989, *Relativistic Fluids and Magnetofluids*, Cambridge University Press, Cambridge, U.K.
Anninos, P., Fragile, P. C., & Salmonson, J. D. 2005, ApJ, 635, 723
Begelman, M. C., Blandford, R. D. & Rees, M. J. 1984, Rev. Mod. Phys., 56, 255
Berger, M. J., & Colella, P. 1989, J. Comput. Phys., 82, 64
Berger, M. J. & Oliger, J. 1984, J. Comput. Phys., 53, 484
Blandford, R. D., McKee, C. F., & Rees, M. J. 1977, Nature, 267, 211
Bryan, G. L. & Norman, M. L. 1997a, arXiv:astro-ph/9710187
Bryan, G. L. & Norman, M. L. 1997b, ASP Conf. Ser. 123: Computational Astrophysics; 12th Kingston Meeting on Theoretical Astrophysics, 123, 363
Bryan, G. L., Abel, T., & Norman, M. L. 2001, arXiv:astro-ph/0112089
Centrella, J. & Wilson, J. R. 1984, ApJS, 54, 229
Colella, P. & Woodward, P. R. 1984, J. Comput. Phys., 54, 174
Del Zanna, L. & Bucciantini, N. 2002, A&A, 390, 1177
Donat, R., Font, J. A., Ibáñez, J. M. & Marquina, A. 1998, J. Comput. Phys., 146, 58
Gehrels, N. et al. 2004, ApJ, 611, 1005
Gingold, R. A., & Monaghan, J. J. 1977, MNRAS, 181, 375
Harten, A., Lax, P. D. & van Leer, B. 1983, SIAM Rev., 25, 35

Hawley, J. F., Wilson, J. R., & Smarr, L. L. 1984, ApJ, 277, 296
Hawley, J. F., Wilson, J. R., & Smarr, L. L. 1984, ApJS, 55, 211
Hughes, P. A., Miller, M. A., & Duncan, G. C. 2002, ApJ, 572, 713
Jiang, G.-S. & Shu, C.-W. 1996, J. Comput. Phys., 126, 202
Kurganov, A. & Tadmor, E. 2000, J. Comput. Phys., 160, 241
Kurganov, A., Noelle, S. & Petrova, G. 2001, SIAM J. Sci. Comput., 23, 707
LeVeque, R. J. 2002, *Finite Volume Methods for Hyperbolic Problems* (Cambridge University Press)
Lithwick, Y. & Sari, R. 2001, ApJ, 555, 540
Liu, X.-D. & Osher, S. 1998, J. Comput. Phys., 142, 304
Lucas-Serrano, A., Font, J. A., Ibáñez, J. M., & Martí, J. M. 2004, A&A, 428, 703
Lucy, L. B. 1977, ApJ, 82, 1013
Martí, J. M. & Müller, E. 1994, J. Fluid Mech., 258, 317
Martí, J. M. & Müller, E. 1996, J. Comput. Phys., 123, 1
Marti, J. M. A., Mueller, E., Font, J. A., Ibanez, J. M. A., & Marquina, A. 1997, ApJ, 479, 151
Martí, J. M. & Müller, E. 2003, Living Reviews in Relativity, 6, 7
Meliani, Z., Keppens, R., Casse, F. & Giannios, D. 2006, ArXiv preprint: astro-ph/0701434
Mignone, A. & Bodo, G. 2005, MNRAS, 364, 126
Mignone, A., Plewa, T., & Bodo, G. 2005, ApJS, 160, 199
Mirabel, I. F. & Rodriguez, L. F. 1994, Nature, 371, 46
Morsony, B. J., Lazzati, D., & Begelman, M. C. 2006, ArXiv Astrophysics e-prints, arXiv:astro-ph/0609254

Norman, M. L., & Winkler, K.-H. A. 1986, NATO Advanced Research Workshop on Astrophysical Radiation Hydrodynamics, 449, Eds. Karl-Heinz A. Winkler, Michael L. Norman

O'Shea, B. W., Bryan, G., Bordner, J., Norman, M. L., Abel, T., Harkness, R., & Kritsuk, A. 2004, In "Adaptive Mesh Refinement - Theory and Applications", Eds. T. Plewa, T. Linde & V. G. Weirs, Springer Lecture Notes in Computational Science and Engineering, 2004

Quirk, J. 1994, Int. J. Numer. Methods Fluids, 18, 555

Pons, J. A., Martí, J. M. & Müller, E. 2000, J. Fluid Mech., 422, 125

Schneider, V., Katscher, U., Rischke, D. H., Waldhauser, B., Maruhn, J. A. & Munz, C.-D. 1993, J. Comput. Phys., 105, 92

Shu, C.-W. & Osher, S., 1988, J. Comput. Phys., 77, 439

Tingay, S. J. et al. 1995, Nature, 374, 141.

Toro E. F., Spruce M. & Speares W. 1994, Shock Waves, 4, 25

Van Leer, B. 1977, J. Comput. Phys., 23, 276

Van Leer, B. 1979, J. Comput. Phys., 32, 101

Wilson, J. R. 1972, ApJ, 173, 431

Zhang, W. & MacFadyen, A. I. 2006, ApJS, 164, 255